

STEREO measurements of electron acceleration beyond fast Fermi at the bow shock

M. P. Pulupa,¹ S. D. Bale^{1,2}, A. Opitz³, A. Fedorov³, R. P. Lin^{1,4}, J.-A.

Sauvaud³

M. P. Pulupa, Space Sciences Laboratory, University of California, 7 Gauss Way, Berkeley, CA 94708, USA. (pulupa@ssl.berkeley.edu)

S. D. Bale, Department of Physics and Space Sciences Laboratory, University of California, 7 Gauss Way, Berkeley, CA 94708, USA. (bale@ssl.berkeley.edu)

A. Opitz, IRAP-Université de Toulouse, CNRS, 9 av. du colonel Roche, BP 44346, 31028 Toulouse Cedex 4, France (andrea.opitz@cesr.fr)

A. Fedorov, IRAP-Université de Toulouse, CNRS, 9 av. du colonel Roche, BP 44346, 31028 Toulouse Cedex 4, France (fedorov@cesr.fr)

R. P. Lin, Space Sciences Laboratory, University of California, 7 Gauss Way, Berkeley, CA 94708, USA. (rlin@ssl.berkeley.edu)

J.-A. Sauvaud, IRAP-Université de Toulouse, CNRS, 9 av. du colonel Roche, BP 44346, 31028 Toulouse Cedex 4, France (jeanandre.sauvaud@cesr.fr)

¹Space Sciences Laboratory, University of California, Berkeley, California, USA

²Physics Department, University of California, Berkeley, California, USA

Abstract. Solar wind electrons are accelerated and reflected upstream by the terrestrial bow shock into a region known as the electron foreshock. Previously observed electron spectra at low energies are consistent with a fast Fermi mechanism, based on the adiabatic conservation of the magnetic moment (μ) of the accelerated electrons. At higher energies, suprathermal power law tails are observed beyond the level predicted by fast Fermi.

The SWEA and STE electron detectors on STEREO enable measurements of foreshock electrons with good energy resolution and sensitivity over the entire foreshock beam. We investigate the electron acceleration mechanism by comparing observed STEREO electron spectra with predictions based on a Liouville mapping of upstream electrons through a shock encounter. The foreshock electron beam extends up to several tens of keV, energies for which the Larmor radii of electrons is tens of km or greater. These radii are comparable to the scale sizes of the shock, and μ conservation no longer applies. We show that the observed enhancement in the foreshock beam beyond fast Fermi levels begins at energies where this assumption breaks down.

³IRAP (CNRS-UPS), University of
Toulouse, Toulouse, France

⁴School of Space Research, Kyung Hee
University, Yongin, Korea

We also demonstrate, using the Liouville mapping technique, that the strahl plays an important role in the formation of the bump on tail instability. We discuss this in the context of recent observations in the foreshock and in solar wind magnetic holes.

1. Introduction

The region of interplanetary space which is upstream of the terrestrial bow shock and magnetically connected to the shock is known as the foreshock. Observations of upstream electron beams [Anderson *et al.*, 1979; Feldman *et al.*, 1983; Gosling *et al.*, 1989] near the leading edge of the foreshock demonstrated that incident solar wind electrons are accelerated by the quasiperpendicular bow shock back into the interplanetary medium. These electron beams are frequently associated with electrostatic Langmuir oscillations. Filbert and Kellogg [1979] pointed out that the effect of velocity dispersion of accelerated electrons convecting downstream with the solar wind is to create bump on tail electron velocity distribution functions (eVDFs). The bump on tail eVDFs are then unstable to the growth of Langmuir waves via Landau resonance.

The canonical picture of the quasiperpendicular electron acceleration process is the Fast Fermi model developed by Leroy and Mangeney [1984] and Wu [1984], which treats the electron-shock encounter assuming conservation of the first adiabatic invariant ($\mu = mv_{\perp}^2/2B$) in the de Hoffmann-Teller (HT) frame. In the HT frame, the upstream bulk velocity \mathbf{u}_u and magnetic field \mathbf{B}_u are parallel, and the electrons do not encounter a motional electric field. The transformation velocity v_{HT} to the HT frame from any shock stationary frame lies in the plane of the shock and is given by

$$\mathbf{v}_{\text{HT}} = \frac{\hat{\mathbf{n}} \times (\mathbf{u}_u \times \mathbf{B}_u)}{\mathbf{B}_u \cdot \hat{\mathbf{n}}} \quad (1)$$

In this picture, the energization is a consequence of the boost to the HT frame, the mirroring, and the boost back to the solar wind frame. The accelerated electrons gain

parallel velocity proportional to $2v_{HT}$. Detailed expressions for the eVDFs upstream of the shock in the foreshock region have been presented by *Cairns* [1987] and *Fitzenreiter et al.* [1990]. A review of the physics of electron acceleration at the bow shock is presented in *Burgess* [2007].

The fast Fermi theory works well to describe relatively low energy electron acceleration. Observed features of foreshock electrons such as prominent bump on tail eVDFs [*Fitzenreiter et al.*, 1984, 1996] and energy dependent loss cone widths [*Larson et al.*, 1996] can be explained in the context of the theory and used to deduce information about the shock at the acceleration site. Simulations of electron interactions with planar and curved shocks [*Krauss-Varban et al.*, 1989; *Krauss-Varban and Burgess*, 1991] also agree well with the fast Fermi model.

However, for the more energetic electrons observed in the foreshock (for example, the > 16 keV electrons in Figure 2 of *Anderson et al.* [1979], and the power law tails observed by *Gosling et al.* [1989] and *Oka et al.* [2006]), the assumptions used in the fast Fermi model are inapplicable. Electrons with energies of tens of keV or higher have Larmor radii r_{Le} which are comparable to the ion Larmor radius r_{Li} and/or the ion inertial length c/ω_{pi} in the solar wind at 1 AU. Since the scale size of the quasiperpendicular bow shock is set by these ion scales [*Bale et al.*, 2003], the conditions for μ conservation are violated, and the presence of the observed suprathermal electrons must be explained by physics beyond single encounter fast Fermi acceleration.

This study presents STEREO observations of foreshock electron beams with good energy resolution over the entire energy range of the beams. Section 2 describes the STEREO instrumentation, and Section 3 describes the fitting procedure for the incident population

of solar wind electrons. Section 4 discusses the method of Liouville mapping the incident eVDF through the shock encounter. The Liouville mapping predictions are compared with observations in Section 5, and the impact of the results on the theory of electron shock acceleration are discussed. Section 6 summarizes the conclusions of this study.

2. STEREO Measurements

2.1. Overview

During the early part of the STEREO mission, both spacecraft spent significant time in the terrestrial electron foreshock. Upstream Langmuir waves [*Malaspina et al.*, 2009] and electron beams were observed over distances of several hundred R_E upstream of the shock. This paper focuses on one foreshock event, which occurred at approximately 0730 UT on 20 December 2006. At this time, the spacecraft GSE coordinates were approximately $[77.9, -64.4, -10.8]R_E$.

Langmuir wave observations were made with the S/WAVES LFR instrument [*Bougeret et al.*, 2008], which measures electric field fluctuations from 2.5 to 160 kHz, a range which includes the local plasma frequency. Magnetic field measurements were made with the STEREO/IMPACT MAG instrument [*Luhmann et al.*, 2008; *Acuña et al.*, 2008]. Solar wind and foreshock electron observations were made with the STEREO/IMPACT electron detectors. The instruments used were the electrostatic SWEA detector [*Sauvaud et al.*, 2008], which measures electrons from 1 eV to 2 keV with nearly 4π angular coverage, and the solid state detector STE [*Lin et al.*, 2008], which measures electrons from 2 keV to 100 keV. Together, these detectors span the energy range of the known populations of quiet time solar wind electrons [*Lin*, 1998].

An overview plot of the foreshock event is shown in Figure 1. From top to bottom, Figure 1 shows the magnetic field in GSE coordinates, the LFR electric field spectrogram, an energy spectrogram from the STE D3 detector, STE pitch angle distributions (PADs) at 13.6 keV and 5.2 keV, and SWEA PADs at 1060 eV and 400 eV. For the entire event, the x_{GSE} component of the magnetic field is negative, which implies that electrons with pitch angles close to 0° are traveling towards the bow shock (i.e., incident to the shock) and those with pitch angles close to 180° are traveling sunward (i.e., backstreaming from the shock).

Three time intervals are indicated in Figure 1. During the first interval (indicated by two solid vertical lines), from 0720 to 0722 UT, the spacecraft was in the undisturbed solar wind, unconnected to the bow shock. The electron PADs for this time period show evidence of a beam-like strahl population, apparent as an enhancement in pitch angles close to 0° in the 400 eV PAD.

The spacecraft then enters the electron foreshock. Starting just before 0725 UT, foreshock electron beams appear as enhancements in pitch angles close to 180° . The foreshock electron beams are visible in the SWEA and STE PADs. Bursty beam-driven Langmuir wave emission at around 19 kHz is also apparent. The STE energy spectrogram shows that the foreshock electron beam evolves rapidly. This evolution is an expected and previously observed consequence of the time-of-flight velocity dispersion in the foreshock [*Filbert and Kellogg, 1979*].

The second and third time intervals (indicated in Figure 1 by vertical dashed lines) show observations at two different foreshock depths. During the first interval at 07:25, the spacecraft is close to the foreshock edge, and the foreshock beam energy spectrum

reaches well into the STE energy range. During the second interval at 07:27, the spacecraft is deeper in the foreshock and the foreshock beam is at lower energies. These intervals will be examined in detail in Section 5.

2.2. Interpretation of STE observations

The STE instrument has two sensor units, each consisting of a set of four thin window silicon semiconductor detectors. The two units are centered along the nominal Parker spiral in the upstream (STE-U) and downstream (STE-D) directions. [Lin *et al.*, 2008; Wang *et al.*, 2010].

Because the central look detection of each STE angular bin lies in the ecliptic, the pitch angle coverage of the STE instrument depends on the magnetic field observed at the spacecraft. For example, if the field is entirely in the \mathbf{z}_{GSE} direction, each STE detector observes the same pitch angle (90°). If the field is in the $\mathbf{x}_{\text{GSE}} - \mathbf{y}_{\text{GSE}}$ plane, more pitch angle information can be recovered. Evidence of this dependence is visible in the STE PAD plots in Figure 1, which demonstrate considerably wider range in pitch angle as the \mathbf{z}_{GSE} component of the field decreases.

When STEREO is in its normal orientation with the SECCHI imagers [Howard *et al.*, 2008] looking at the sun (which is the case for the entire mission, excepting some early orbital maneuvers and short, isolated magnetometer calibration intervals), multiply reflected solar optical and UV light contaminates the STE-U detectors. For this reason, only STE-D data is presented in this paper.

Because the detectors are open, without curved path electrostatic deflectors or foil covers, STE measures ions, neutrals [Wang *et al.*, 2010], and X-rays [Hsieh *et al.*, 2009] in addition to electrons. For this reason, we must be careful in interpreting STE data in the

foreshock region. In order to be assured that an observed STE signal is indeed a foreshock electron beam, we require both (a) simultaneous electron measurements from SWEA and (b) associated Langmuir wave activity. The STE observations themselves must also be consistent with electron beams. An example of STE data which is inconsistent with foreshock electron beams is visible in Figure 1 at 07:34 UT. Were the measured spectra at these times due solely to electrons, the features observable in the STE spectrogram at several tens of keV would be highly unstable, so the electron measurement at these times is likely contaminated by foreshock ions.

The two foreshock intervals highlighted in Figure 1 have STE spectra consistent with electrons, simultaneous SWEA observations, and associated S/WAVES Langmuir waves. For the remainder of this paper the observations at these intervals are taken to be foreshock electron beams.

3. Incident electrons

The solar wind electrons comprise several distinct populations; the populations considered in this paper are the core, the halo, the strahl, and the superhalo. The thermal core population makes up most of the number density of the solar wind and can be modeled well using a bi-Maxwellian distribution. The suprathermal halo population is better described by a bi- κ distribution, which resembles a bi-Maxwellian at low energies and behaves like a power law distribution at high energies [*Maksimovic et al.*, 1997]. The strahl component of the solar wind is a beam-like feature propagating along the magnetic field in the antisunward direction. A detailed description of the core, halo, and strahl components can be found in *Štverák et al.* [2009].

In addition to the above components, the quiet time solar wind electrons include a population known as the superhalo, which can be approximated using a power law from energies of several keV up to 100 keV [*Lin et al.*, 1996; *Wang et al.*, 2012]. The superhalo electrons have been shown to be nearly isotropic [*Lin*, 1998].

The energy spectrum and the PAD of the incident solar wind electrons are shown in the top row of Figure 2. Electrons from 57.5 eV to 1.1 keV are measured by the SWEA instrument and are marked with asterisks. SWEA exhibits a degradation in low energy electron measurements due to instrumental charging effects [*Fedorov et al.*, 2011], so the energies below 50 eV are not plotted in Figure 2. SWEA measurements above 50 eV are corrected by the transmission function described in *Fedorov et al.* [2011]. The incident PAD shown in Figure 2 shows evidence of a strong strahl beam (the peak near zero pitch angle) and a relatively isotropic halo population (the relatively flat lines at pitch angles greater than 90°).

Electrons from 2 keV to 100 keV are measured by STE and are marked with diamonds. During the time interval when the incident electrons were measured, the magnetic field contained a strong component in the \mathbf{z}_{GSE} direction, and the angular coverage of the STE instrument was limited to a narrow range of pitch angles. For clarity, not all of the STE electron energy bins are shown.

Incident energy spectra at near-parallel (green) and near-perpendicular (blue) pitch angles are shown in the top left of Figure 2, again plotted with asterisks for SWEA and diamonds for STE. For SWEA, the blue perpendicular cut measurements are measured with bins with a pitch angle of 90° , while the green parallel cut measures electrons with pitch angle of 37° . We do not use the pitch angle closest to 0° , as these electrons will likely

lie inside the loss cone and, according to the fast Fermi theory, will not be accelerated by the shock. The lack of pitch angle coverage from the STE instrument during this time interval limits the ability to choose near-parallel and near-perpendicular cuts. This is mitigated by the fact that the quiet time superhalo is nearly isotropic [Lin, 1998].

The blue and green solid lines on the incident energy spectrum plot in Figure 2 are the results of fitting the eVDF to a model including the core, the halo, the strahl, and the superhalo. Each individual population is shown as a dotted line. The blue (perpendicular) solid line is the sum of the core, halo, and superhalo populations. The green (parallel) solid line is the sum of the blue line and the strahl population.

Due to the previously mentioned instrumental charging effects, SWEA measurements of the core population are limited. To characterize the core, we instead use convected electron measurements from the SWE instrument on board the *Wind* spacecraft Ogilvie *et al.* [1995], calculating the time lag according to the method described in Opitz *et al.* [2009]. The time-shifted core density n_c is $4.72/\text{cm}^3$, and the core electron temperature T_c is 8.82 eV. This density corresponds to a local plasma frequency of ~ 19.6 kHz, which matches the frequency of the observed LFR Langmuir waves.

The halo component for this interval is well represented by an isotropic κ distribution. The strahl component is modeled by subtracting the near-perpendicular SWEA cut from the near-parallel SWEA cut, then fitting the excess parallel observation as a function of energy using a spline fit. The superhalo is fitted with a modified κ -type distribution which accounts for the relativistic behavior of the highest energy electrons [Xiao, 2006; Pierrard and Lazar, 2010]. It is assumed that the quiet-time superhalo is isotropic.

The model eVDF matches the data well over the range of the halo, strahl, and superhalo. The parameters for the fitted eVDFs are summarized in Table 1.

4. Predicted foreshock electron properties

As stated above, the aim of this paper is to compare observed foreshock electron observations to the canonical Fast Fermi theory of electron acceleration. In order to use this theory to predict the properties of a foreshock electron beam, information about (a) the shock parameters, (b) the interaction of the electrons with the shock, and (c) evolution of the beam is necessary. In this section, we discuss the estimation of these quantities.

4.1. Shock parameters

According to Fast Fermi theory, the acceleration of an electron by the bow shock depends on the loss cone angle α , which is determined by the magnetic mirror ratio between the upstream magnetic field and the field in the shock front, the HT speed v_{HT} , and the cross shock potential Φ . In order to determine the eVDF at an arbitrary point in the foreshock region, it is also necessary to know the depth of the spacecraft in the foreshock region, since the depth determines the cutoff electron speed v_c necessary for an electron to reach the spacecraft (electrons with $v < v_c$ will be convected downstream by the motional electric field of the solar wind and will not be observed at the spacecraft [*Anderson et al.*, 1979; *Filbert and Kellogg*, 1979; *Cairns*, 1987]).

None of these parameters can be directly measured when the spacecraft is far from the shock. On 20 December 2006, STEREO/B was approximately $100 R_E$ from of the Earth's bow shock, and several days had passed since its previous bow shock crossing. Furthermore, the location of that previous crossing was not close to the quasiperpendicular

connection point at which the electron acceleration takes place. For these reasons, α and Φ cannot be accurately estimated using data from the previous STEREO shock crossing. Previous papers dealing with electron acceleration at the bow shock (e.g., *Filbert and Kellogg* [1979]; *Larson et al.* [1996]) have used the straight field line approximation to determine θ_{bn} , which yields v_{HT} , and depth in the foreshock, which yields v_c . However, with a spacecraft more than several tens of R_E upstream of the bow shock, magnetic field line wandering makes such an assumption invalid [*Zimbardo and Veltri*, 1996]. We must therefore estimate the relevant parameters using different methods.

The ratio of the maximum field in the shock layer (including any overshoot) to the upstream field B_{max}/B_u determines the opening angle α of the fast Fermi loss cone. We use data from the Geotail spacecraft to estimate this parameter. On 20 December 2006 at approximately 15:00 UT, Geotail observed several crossings of the quasiperpendicular bow shock at GSE coordinates of approximately $[2.7, -17.6, 3.8]R_E$, i.e., in the neighborhood of the point where the STEREO/B spacecraft was connected to the shock some hours earlier. Although this conjunction is only approximate in both time and space, the Geotail data nevertheless give a picture of the typical conditions of the quasiperpendicular shock during the relevant time interval. Figure 3 shows magnetic field data from the Geotail MGF instrument [*Kokubun et al.*, 1994] on 20 Dec 2006. The quasiperpendicular shock crossings are seen as rapid changes in $|B|$. The ratio B_{max}/B_u is measured for several shock crossings and shown above the plot. The ratios range from under 4 to slightly over 5, with an average B_{max}/B_u of 4.64. Using the relation $\sin^2 \alpha = B_u/B_{max}$ to compute the loss cone angle yields $\alpha = 27.7^\circ$.

In order to estimate Φ , we use the result of an analytical model [*Kuncic et al.*, 2002] for the cross shock potential which depends only on the upstream perpendicular electron temperature and the magnetic compression ratio.

$$e\Phi \simeq 2kT_{e\perp u} \left(\frac{B_d}{B_u} - 1 \right) \quad (2)$$

This model has been shown to be consistent with spacecraft measurements of electron temperature made during bow shock crossings [*Hull et al.*, 2000]. Using the convected *Wind* electron measurements, the Geotail magnetic field, and Equation (2), we estimate the cross shock potential $\Phi \approx 72$ V.

The v_{HT} parameter must be estimated from the foreshock electron data. Since electrons gain energy proportional to $2v_{HT}$, the energy gain of the electrons can be used to estimate v_{HT} , using the Liouville mapping technique described in the following section. We use the relatively low energy SWEA electron energy bins to estimate v_{HT} , by matching observed fluxes with predictions based on the upstream measurements. For the 07:25 UT interval at the foreshock edge, the estimated v_{HT} is 1500 km/s. For the 07:27 UT interval, the estimated v_{HT} is 500 km/s. Similarly, v_c can be estimated from the foreshock data by observing the lowest energy bin which shows evidence of foreshock electrons. The estimated values of v_c for the 07:25 foreshock edge interval and the 07:27 interval are 13000 km/s and 4250 km/s, respectively.

The estimated Fast Fermi parameters α , Φ , v_{HT} , and v_c are listed in Table 2.

4.2. Liouville mapping

Liouville's theorem states that, in the absence of collisions, the phase space density f of a collection of particles remains constant along a trajectory defined by the (conservative and differentiable) forces which govern the system. In the case of the solar wind electrons, this implies that f_i for the incident eVDF remains constant along trajectories determined by the fast Fermi theory, so long as that theory remains applicable. The theorem allows for the prediction of foreshock eVDFs given the upstream observations and the shock parameters estimated above.

The Liouville theorem is the basis behind previous theoretical work predicting foreshock eVDFs [e.g. *Cairns*, 1987; *Fitzenreiter et al.*, 1990]. It has also been used in experimental studies analyzing the evolution of the eVDF through bow shock crossings [*Gosling et al.*, 1989; *Hull et al.*, 2001; *Lefebvre et al.*, 2007]. In the HT frame, electrons traveling toward the shock which satisfy the condition

$$\frac{1}{2}m\frac{v_{\perp}^2}{B_u} \geq \frac{1}{B_d - B_u} \left(e\Phi' + \frac{1}{2}mv_{\parallel}^2 \right) \quad (3)$$

will be reflected by the shock, assuming conservation of the adiabatic invariant μ (see, e.g., *Knock et al.* [2001, Eq. 9]). In the HT frame, these electrons reverse the sign of their parallel velocity, which adds a parallel velocity of $2v_{HT}$. A schematic diagram of fast Fermi acceleration which combines the illustrations of *Leroy and Mangeney* [1984] and *Wu* [1984] is shown in Figure 1 of *Pulupa et al.* [2010].

In order to be observed at the spacecraft, the electrons must additionally meet the criterion that their parallel velocity is higher than the geometric cutoff velocity at the spacecraft. The Liouville mapping of the incident eVDF f_i to the foreshock eVDF f_f can then be summarized in the following equation:

$$f_{\text{f}}(v_{\parallel}, v_{\perp}) = \begin{cases} f_{\text{i}}(v_{\parallel}, v_{\perp}) & v_{\parallel} < \max[v_{\text{c}}, v_{\text{HT}}] \\ f_{\text{i}}(v_{\parallel}, v_{\perp}) & v_{\parallel} > \max[v_{\text{c}}, v_{\text{HT}}], \\ & \text{in loss cone} \\ f_{\text{i}}(2v_{\text{HT}} - v_{\parallel}, v_{\perp}) & v_{\parallel} > \max[v_{\text{c}}, v_{\text{HT}}], \\ & \text{reflected} \end{cases} \quad (4)$$

Using Equations 3 and 4, we can directly calculate the predicted foreshock eVDFs given by Fast Fermi theory, and observe deviations from the measured STEREO data.

4.3. Quasilinear relaxation

Foreshock electron beams can create a bump on tail feature which is unstable to the growth of Langmuir waves on very short time scales. The foreshock beam is unstable when the reduced parallel distribution $f_{\parallel}(v_{\parallel})$ displays a positive slope in the v_{\parallel} direction ($\partial f_{\parallel}/\partial v_{\parallel} > 0$). In the quasilinear theory of beam relaxation [Groganard, 1975; Muschietti, 1990; Robinson and Benz, 2000], positive slopes in the eVDF are mediated by Landau resonance, which generates Langmuir waves. In short order, the region around the bump on tail evolves to a marginally stable ($\partial f_{\parallel}/\partial v_{\parallel} \approx 0$) plateaued state.

In this work, the method of Knock *et al.* [2001] and Kuncic *et al.* [2004] is used in order to estimate the region over which the flattening of the beam will occur. The procedure is as follows: Using the foreshock eVDF obtained from the Liouville mapping, the reduced distribution f_{\parallel} is constructed. The bump on tail is flattened by solving numerically for the points v_{-} and v_{+} which satisfy the conditions that $f_{\parallel}(v_{-}) = f_{\parallel}(v_{+})$ and the number of particles $\int_{v_{-}}^{v_{+}} f_{\parallel} dv_{\parallel}$ is conserved. The velocity of the beam v_{b} and its width Δv_{b} can then be calculated from v_{-} and v_{+} .

5. Foreshock electrons

Energy spectra and PADs for the foreshock electrons are shown in the middle and bottom rows of Figure 2, with the foreshock edge observations in the middle row and the deeper foreshock observations in the bottom row. As in the top row, energy spectra are to the left, PADs are to the right, SWEA data is plotted with asterisks, and STE data with diamonds. The foreshock beam is evident in the foreshock PADs as an enhancement (compared to the solar wind PAD) for angles greater than 90° . Near-perpendicular and near-antiparallel (backstreaming) cuts through the eVDF are plotted in the left panels with blue and red solid lines. The solid lines plotted along with the electron spectra are the results of the Liouville mapping.

We analyze two intervals in order to emphasize different aspects of the foreshock electron beam. Using the foreshock edge observations, we can isolate and examine the behavior of the high energy suprathermal foreshock beam electrons, lower energy electrons having been cut off from the beam by the foreshock geometry. Using the deeper foreshock observations we can observe the lower energy foreshock beam. These energies are useful for analyzing the effect of the strahl population and the limitations of the fast Fermi theory.

5.1. Foreshock edge

The foreshock edge observations from 07:25 UT are shown in the middle row of Figure 2. For reference, the incident/strahl population line from the top row is also plotted on this spectrum as a green solid line. A foreshock beam consisting of electrons which were simply reflected without energization would lie directly atop the green line. Electron measurements showing evidence of energization therefore lie above the green line. The electron beam in the foreshock edge energy spectrum is evident from the SWEA energy bin at 1.1 keV up to the 20 keV STE energy bin. In terms of the Liouville mapping,

this implies that the velocity cutoff is somewhere below 1.1 keV, and that v_{HT} can be determined by matching the observed beam at 1.1 keV to Liouville map predictions. For the foreshock edge, we find $v_c \approx 13000$ km/s, and $v_{\text{HT}} \approx 1500$ km/s. However, it is clear that the Liouville predictions do not match the STE observations at higher energies.

This result is consistent with observations of *Gosling et al.* [1989], who noted that a Liouville mapping predicting the downstream eVDF differed significantly from observations. Additional processes beyond μ -conserving reflection must apply for these suprathermal energies.

Figure 4 shows only the parallel STE data from the foreshock edge energy spectrum of Figure 2. The solid red line is the predicted spectrum using the fast Fermi model, as is also shown in Figure 2. The red shaded area in Figure 4 brackets the model predictions with extreme values of v_{HT} . Varying v_{HT} between 0 and 10000 km/s yields the lower and upper boundaries of the shaded area, respectively. It is clear that both the level and shape of the observed spectrum differs from the model predictions for the low and high values of v_{HT} , emphasizing that the departure of the observations from fast Fermi is not simply a consequence of parameter choice. The data are fit to a power law with an exponential roll-off, following *Oka et al.* [2006]. For this particular interval near the foreshock edge, we find a relatively energetic power law, with a power law index Γ of 2.04 and a roll-off energy E_0 of 5.5 keV. The power law index and rollover energy evolve as a function of time with variation in the electron beam, and the relationship between Γ and E_0 may be the subject of a future study.

5.2. Mechanisms for high energy electrons

Previously, *Gosling et al.* [1989] noted that observed electron fluxes could not be adequately explained by the fast Fermi mechanism, and suggested that the suprathermal upstream electrons could be leaked from a downstream population which had been accelerated by the shock. For the mechanism for generation of the observed enhancements in suprathermal electrons, *Gosling et al.* [1989] proposed shock drift acceleration. Shock drift theory has been shown to be equivalent to the fast Fermi mechanism [*Krauss-Varban and Wu*, 1989] for single encounters, but also can be naturally extended to study multiple encounters between the electron and the shock [*Ball and Melrose*, 2001]. Shock drift theory [*Vandas*, 2001] has been used to study the parametric dependence of upstream electrons on shock parameters, and to compare observed and predicted spectra. The results are qualitatively similar but suggest that additional processes are important, especially for the high energy (above 10 keV) electrons.

More recently, several alternative ideas have been proposed, which explain the enhanced suprathermal electrons as a consequence of some type of process which can create pitch angle scattering in an incident electron [*Burgess*, 2007]. The scattered trajectory enables the electron to make multiple encounters with the shock and be accelerated to high energies. We briefly describe several proposed processes in the paragraphs below.

Recent simulation work has also considered the effect of non-ideal structure on shock fronts on suprathermal electron acceleration. Using hybrid simulations and an injection profile of 100 eV electrons, *Burgess* [2006] investigated several effects of shock front ripples, finding a considerable increase of the electron maximum energy and electron acceleration from a broader range of θ_{bn} than was the case for planar shocks. The difference in the interaction between a rippled and a planar shock lies in the ability of electrons to encounter

the shock multiple times, due to the connection of a magnetic field line to multiple points on the surface of a rippled shock. Evidence of such multiply connected electron acceleration sites (although for larger length scales than studied by *Burgess* [2006]) has been observed at CME-driven interplanetary shocks and is related to the generation of Type II radio bursts [*Bale et al.*, 1999; *Pulupa and Bale*, 2008].

Previous Geotail observations of energetic electrons show a connection between energetic electrons and upstream whistler waves [*Oka et al.*, 2006], showing a dependence of foreshock electron power law index on the whistler critical Mach number. This dependence has been explained as accelerated foreshock electron beams generating wave activity which can scatter electrons back and forth across the shock in a mechanism akin to the diffusive shock acceleration observed in the ion foreshock [*Amano and Hoshino*, 2010]. In a single event analysis using data from a Geotail shock crossing, a gradual (as opposed to spiky) temporal profile of accelerated electrons combined with observed upstream whistlers has been observed [*Oka et al.*, 2009].

Guo and Giacalone [2010] investigated the effects of upstream turbulence, also using hybrid simulations. Using test particle trajectories, *Guo and Giacalone* [2010] directly demonstrated the effect of multiple shock crossings on electron energization. *Guo and Giacalone* [2010] also found that the level of upstream turbulence affected the maximum attainable energy for an injection profile of 100 eV electrons, as higher levels of turbulence increased field line wandering and thus the effect of multiple shock encounters.

Savoini and Lembège [2001] and *Savoini et al.* [2010] have used two dimensional particle simulation to directly simulate electron acceleration at the terrestrial bow shock. By tracing test particle orbits, several different types of accelerated electrons are found,

including a population of electrons consistent with Fast Fermi and populations which are temporarily trapped in the front or escaped downstream. The latter populations make up the higher-energy portion of the foreshock beam observed in the simulations, and possibly correspond to the high energy power law tails observed in the hybrid codes and in observations.

Recent work on quasiperpendicular shocks shows evidence of nonstationarity driven by reflected ions on the time scale of the ion gyroperiod causing the shock front to self-reform dynamically [Krasnoselskikh *et al.*, 2002; Lobzin *et al.*, 2007; Lembège *et al.*, 2009]. Lembège and Savoini [2002] have suggested nonstationarity as an explanation for the bursty nature of upstream electron events. The nonstationarity on the shock front, which in simulation results generates a highly non-uniform shock surface, could provide a mechanism for the multiple encounters which can generate high energy electrons.

In future work, observations such as those presented in this paper may be of use in discriminating between the various mechanisms described above. With the STE detector, parameters of the suprathermal electron spectrum such as Γ and E_0 can be studied with good energy resolution up to the highest beam energies. Systematic variation of these parameters with solar wind and shock parameters may vary differently among the proposed mechanisms described in this section, and comparison with observations may therefore offer insight into the physics of electron acceleration.

5.3. Limit of Fast Fermi

The foreshock edge beam examined above exhibited a high velocity cutoff. As a consequence, the lower energy bins were not observed in the foreshock beam. Deeper in the foreshock, the foreshock electron beam extends to lower energies. For the observations

from 07:27 UT, shown in the bottom row of Figure 2, the electron beam is apparent in the energy spectrum from below 100 eV and up to the first several STE energies at several keV. Using the same method of estimating velocity parameters as used in the previous section, we find $v_c \approx 4250$ km/s, and $v_{HT} \approx 500$ km/s for the deeper foreshock measurements.

Using the parameters from Table 2, we can again compare the fast Fermi predictions with the observed data. The Liouville-mapped data (red line) fits the observations (red asterisks) well for the relatively low energy SWEA bins from 151 to 400 eV, with an energy beam which is slightly enhanced compared to the incident strahl population from the top row (green line). This enhancement is consistent with fast Fermi acceleration. However, an additional enhancement in the foreshock electron beam beyond anything consistent with Fast Fermi theory begins in the 650 eV SWEA energy bin.

For typical conditions at the terrestrial bow shock, the combined SWEA and STE energy range covers the transition between adiabatic and non-adiabatic electrons, as the electron gyroradii for electrons with energies of tens of eV are generally much smaller than the shock scale (defined by the ion inertial length or ion gyroradius [*Bale et al.*, 2003]), while the electron gyroradii at tens of keV are comparable to or greater than these lengths. Using convected Wind measurements from the SWE Faraday cup instrument, it is possible to estimate the ion Larmor radius and the ion inertial length. For this event, $r_{Li} = 74$ km and $c/\omega_{pi} = 123$ km. Setting the electron Larmor radius to be equivalent to these length scales requires electron energies of 87 keV and 32 keV, respectively. Similarly, an electron with an energy of 650 eV has a gyroradius equivalent to $0.086 r_{Li}$ or $0.143 c/\omega_{pi}$. Since these ion scale lengths define the scale size of the shock, this confirms that the electron

foreshock beam begins to diverge from Fast Fermi at the expected point: when r_{Le} is no longer much smaller than the scale size of the shock ramp and hence μ is not conserved.

We note that *Gosling et al.* [1989] used a Liouville technique to map the upstream eVDF through the shock and compare to the observed downstream eVDF. In Figure 11b of *Gosling et al.* [1989], the comparison between the observed and Liouville-mapped eVDFs shows the same deviation from single encounter fast Fermi theory, with the observed eVDF substantially enhanced beginning at energies of several hundred eV.

5.4. Role of the strahl

Since the cross shock potential at the terrestrial bow shock is typically of the order of the core electron temperature or higher [*Hull et al.*, 2000, 2001; *Kuncic et al.*, 2002; *Lefebvre et al.*, 2007], the foreshock electron beam is constituted primarily of electrons from the suprathermal solar wind populations. Simulations of electron acceleration and the resulting plasma wave activity [*Wu*, 1984; *Krauss-Varban et al.*, 1989; *Krauss-Varban and Burgess*, 1991; *Kuncic et al.*, 2004; *Malaspina et al.*, 2009] model the upstream eVDF as a sum of core and halo populations, where the halo population is represented as either a hotter Maxwellian population or as a κ distribution.

The effect of the geometrical velocity cutoff is to separate the foreshock eVDF into incident solar wind electrons $v_{\parallel} < v_c$ and reflected electrons $v_{\parallel} > v_c$ (See Equation 4). In the case of a backstreaming beam consisting of reflected halo electrons, a significant bump on tail will form only if the incident electrons are strongly accelerated by a high v_{HT} at the acceleration point—that is, only in a narrow region where θ_{bn} is very close to 90° .

In the case of a backstreaming beam where the incident eVDF has a strong strahl component, however, the bump on tail can be more easily formed. If the ratio of strahl density to halo density n_s/n_h is high, even a small energization will result in a significant bump when combined with the effects of the geometric cutoff—the geometric cutoff will produce an eVDF which consists of the incident halo below v_c but the reflected strahl above v_c . A wider range of θ_{bn} connection points will be able to produce bump on tail eVDFs with a strong strahl component present.

This effect is illustrated in Figure 5. Using the eVDF parameters from Table 1, the fast Fermi parameters for the deep foreshock from Table 2, and Equation 4, the reduced distribution f_{\parallel} computed for two cases: one where the strahl population is included in the incident eVDF, and one where it is removed. In each case, a bump on the tail of f_{\parallel} is created by the fast Fermi process. In the case where the strahl beam is included in the eVDF, the bump is higher and the beam is wider. To quantify the difference in the bumps, the width of the beam Δv_b is calculated as described in Section 4.3. A rough estimate for the energy in the electron beam is also calculated, by comparing $n_b v_b^2$ normalized to $n_h v_h^2$. The beam from the eVDF including the strahl population is more than twice as wide in parallel v and has more than three times the beam energy as does the beam from the eVDF without the strahl (see Figure 5).

The geometry of quasiperpendicular connection to the bow shock divides the electron foreshock into two separate wings, and that the strahl population is incident on the shock in only one wing. Given the discussion above, the presence of the reflected strahl in one foreshock wing will lead to an asymmetry in foreshock wave activity. Such asymmetries have been noted, and correctly explained as a result of strahl electrons, using statistical

studies of wave activity in the foreshock of Venus [*Crawford et al.*, 1993, 1998]. Statistical analysis of electron and wave measurements has shown that the asymmetry also exists in the terrestrial foreshock [*Pulupa et al.*, 2011]. Recent results also connect observations of Langmuir waves in solar wind magnetic holes to the presence of a strahl population [*Briand et al.*, 2010]. *Briand et al.* [2010] note that the suprathermal nature of the strahl population allow it to enter the magnetic hole and provide a source population for electron beams. Similarly, the suprathermal nature of the strahl places the strahl electrons above the threshold condition for reflection determined by the cross shock potential Φ . In both the foreshock and in magnetic holes, the strahl adds asymmetry to the eVDF. When the asymmetric eVDF interacts with a magnetic mirror-like structure such as a shock or the edge of a magnetic hole, the asymmetry leads to an enhancement in the bump on tail feature which is responsible for the generation of Langmuir waves.

It is also possible that the microphysics of the generated Langmuir waves may be affected by the presence of the strahl. Recent observations of type III-related Langmuir waves [*Malaspina et al.*, 2011] have pointed to a relationship between electron beam speed and wave polarization. By supplying a relatively high-energy seed population to the acceleration process, the strahl may indirectly affect wave polarization.

6. Summary and Conclusions

We have presented observations of foreshock electron beams using the STEREO spacecraft, combining the SWEA and STE electron instruments to make observations which simultaneously cover the entire range of foreshock electrons with good energy resolution and sensitivity. Analysis of the beam electrons leads to the following conclusions.

Our results are consistent with the canonical Fast Fermi picture of foreshock electron acceleration for low energy electrons. A significant enhancement of electron acceleration begins at energies where the electron gyroradius is a significant fraction (~ 0.1) of the ion gyroradius and/or ion inertial length. The high energy tail of the foreshock electron beam is well fitted by a power law with an exponential roll-off, and extends up to several tens of keV before falling below the level of the background superhalo electron population. As discussed in Section 5.2, a number of possible mechanisms have been shown to produce suprathermal electrons in this energy range.

Presence of the strahl is a significant factor in producing the bump on tail eVDFs which generate Langmuir waves in the electron foreshock. In particular, in upstream regions where the cutoff velocity v_c lies in the halo-strahl energy range, the asymmetry generated by a strong strahl implies that a large v_{HT} is not necessary to produce a significant bump.

The experimental results presented here may be useful for differentiating among the several physical mechanisms of the shock acceleration of electrons. We suggest that simulation and modeling work in the future should include incident electrons featuring realistic strahl and superhalo populations in addition to halo electrons.

Acknowledgments. We are grateful to the STEREO IMPACT, MAG, and S/WAVES instrument teams. We would like to specifically acknowledge gratitude to L. Wang for assistance with the STE data and to R. Gomez-Herrero for assistance with STEREO SEPT data. We also thank I. Shinohara for access to the Geotail MGF data, and B. Maruca and M. Stevens for SWE Faraday cup data. M. Pulupa acknowledges useful discussions with D. Burgess. This work was supported by NASA grant NNX10AM71G, and also supported in part by NASA grants NAS5-03131 and NNX09AG33G. R. Lin was

also supported in part by the WCU grant (R31-10016) funded by the Korean Ministry of Education, Science, and Technology.

References

- Acuña, M. H., D. Curtis, J. L. Scheifele, C. T. Russell, P. Schroeder, A. Szabo, and J. G. Luhmann (2008), The STEREO/IMPACT Magnetic Field Experiment, *Space Sci. Rev.*, *136*, 203–226, doi:10.1007/s11214-007-9259-2.
- Amano, T., and M. Hoshino (2010), A Critical Mach Number for Electron Injection in Collisionless Shocks, *Physical Review Letters*, *104*(18), 181102, doi:10.1103/PhysRevLett.104.181102.
- Anderson, K. A., R. P. Lin, F. Martel, C. S. Lin, G. K. Parks, and H. Reme (1979), Thin sheets of energetic electrons upstream from the earth's bow shock, *Geophys. Res. Lett.*, *6*, 401–404, doi:10.1029/GL006i005p00401.
- Bale, S. D., M. J. Reiner, J.-L. Bougeret, M. L. Kaiser, S. Krucker, D. E. Larson, and R. P. Lin (1999), The source region of an interplanetary type II radio burst, *Geophys. Res. Lett.*, *26*, 1573–1576, doi:10.1029/1999GL900293.
- Bale, S. D., F. S. Mozer, and T. S. Horbury (2003), Density-Transition Scale at Quasiperpendicular Collisionless Shocks, *Physical Review Letters*, *91*(26), 265004, doi:10.1103/PhysRevLett.91.265004.
- Ball, L., and D. B. Melrose (2001), Shock Drift Acceleration of Electrons, *PASA*, *18*, 361–373, doi:10.1071/AS01047.
- Bougeret, J. L., et al. (2008), S/WAVES: The Radio and Plasma Wave Investigation on the STEREO Mission, *Space Sci. Rev.*, *136*, 487–528, doi:10.1007/s11214-007-9298-8.

- Briand, C., J. Soucek, P. Henri, and A. Mangeney (2010), Waves at the electron plasma frequency associated with solar wind magnetic holes: STEREO/Cluster observations, *Journal of Geophysical Research (Space Physics)*, *115*(A14), A12113, doi:10.1029/2010JA015849.
- Burgess, D. (2006), Simulations of Electron Acceleration at Collisionless Shocks: The Effects of Surface Fluctuations, *Astrophys. J.*, , *653*, 316–324, doi:10.1086/508805.
- Burgess, D. (2007), Particle Acceleration at the Earth’s Bow Shock, in *The High Energy Solar Corona: Waves, Eruptions, Particles*, edited by Klein, K.-L. and MacKinnon, A. L., pp. 161–190, Lecture Notes in Physics, Berlin Springer Verlag.
- Cairns, I. H. (1987), The electron distribution function upstream from the earth’s bow shock, *J. Geophys. Res.*, , *92*, 2315–2327, doi:10.1029/JA092iA03p02315.
- Crawford, G. K., R. J. Strangeway, and C. T. Russell (1993), VLF imaging of the Venus foreshock, *Geophys. Res. Lett.*, , *20*, 2801–2804, doi:10.1029/93GL01258.
- Crawford, G. K., R. J. Strangeway, and C. T. Russell (1998), Statistical imaging of the Venus foreshock using VLF wave emissions, *J. Geophys. Res.*, , *103*, 11,985–12,004, doi:10.1029/97JA02883.
- Fedorov, A., A. Opitz, J.-A. Sauvaud, J. G. Luhmann, D. W. Curtis, and D. E. Larson (2011), The IMPACT Solar Wind Electron Analyzer (SWEA): Reconstruction of the SWEA Transmission Function by Numerical Simulation and Data Analysis, *Space Sci. Rev.*, *161*, 49–62, doi:10.1007/s11214-011-9788-6.
- Feldman, W. C., R. C. Anderson, S. J. Bame, S. P. Gary, J. T. Gosling, D. J. McComas, M. F. Thomsen, G. Paschmann, and M. M. Hoppe (1983), Electron velocity distributions near the earth’s bow shock, *J. Geophys. Res.*, , *88*, 96–110, doi:

10.1029/JA088iA01p00096.

Filbert, P. C., and P. J. Kellogg (1979), Electrostatic noise at the plasma frequency beyond the earth's bow shock, *J. Geophys. Res.*, , *84*, 1369–1381, doi:10.1029/JA084iA04p01369.

Fitzenreiter, R. J., A. J. Klimas, and J. D. Scudder (1984), Detection of bump-on-tail reduced electron velocity distributions at the electron foreshock boundary, *Geophys. Res. Lett.*, , *11*, 496–499, doi:10.1029/GL011i005p00496.

Fitzenreiter, R. J., J. D. Scudder, and A. J. Klimas (1990), Three-dimensional analytical model for the spatial variation of the foreshock electron distribution function - Systematics and comparisons with ISEE observations, *J. Geophys. Res.*, , *95*, 4155–4173, doi:10.1029/JA095iA04p04155.

Fitzenreiter, R. J., A. F. Viñas, A. J. Klimas, R. P. Lepping, M. L. Kaiser, and T. G. Onsager (1996), Wind observations of the electron foreshock, *Geophys. Res. Lett.*, , *23*, 1235–1238, doi:10.1029/96GL00826.

Gosling, J. T., M. F. Thomsen, S. J. Bame, and C. T. Russell (1989), Suprathermal electrons at earth's bow shock, *J. Geophys. Res.*, , *94*, 10,011–10,025, doi:10.1029/JA094iA08p10011.

Grognard, R. J.-M. (1975), Deficiencies of the asymptotic solutions commonly found in the quasilinear relaxation theory, *Australian Journal of Physics*, *28*, 731.

Guo, F., and J. Giacalone (2010), The Effect of Large-scale Magnetic Turbulence on the Acceleration of Electrons by Perpendicular Collisionless Shocks, *Astrophys. J.*, , *715*, 406–411, doi:10.1088/0004-637X/715/1/406.

Howard, R. A., et al. (2008), Sun Earth Connection Coronal and Heliospheric Investigation

(SECCHI), *Space Sci. Rev.*, *136*, 67–115, doi:10.1007/s11214-008-9341-4.

Hsieh, K. C., P. C. Frisch, J. Giacalone, J. R. Jokipii, J. Kóta, D. E. Larson, R. P. Lin, J. G. Luhmann, and L. Wang (2009), A Re-Interpretation of STEREO/STE Observations and

Its Consequences, *Astrophys. J.*, , *694*, L79–L82, doi:10.1088/0004-637X/694/1/L79.

Hull, A. J., J. D. Scudder, R. J. Fitzenreiter, K. W. Ogilvie, J. A. Newbury, and C. T.

Russell (2000), Electron temperature and de Hoffmann-Teller potential change across the Earth's bow shock: New results from ISEE 1, *J. Geophys. Res.*, , *105*, 20,957–20,972, doi:10.1029/2000JA900049.

Hull, A. J., J. D. Scudder, D. E. Larson, and R. Lin (2001), Electron heating and phase

space signatures at supercritical, fast mode shocks, *J. Geophys. Res.*, , *106*, 15,711–15,734, doi:10.1029/2001JA900001.

Knock, S. A., I. H. Cairns, P. A. Robinson, and Z. Kuncic (2001), Theory of type II

radio emission from the foreshock of an interplanetary shock, *J. Geophys. Res.*, , *106*, 25,041–25,052, doi:10.1029/2001JA000053.

Kokubun, S., T. Yamamoto, M. Acuña, K. Hayashi, K. Shiokawa, and H. Kawano (1994),

The GEOTAIL Magnetic Field Experiment, *Journal of Geomagnetism and Geoelectricity*, *46*(1), 7.

Krasnoselskikh, V. V., B. Lembège, P. Savoini, and V. V. Lobzin (2002), Nonstationarity

of strong collisionless quasiperpendicular shocks: Theory and full particle numerical simulations, *Physics of Plasmas*, *9*, 1192–1209, doi:10.1063/1.1457465.

Krauss-Varban, D., and D. Burgess (1991), Electron acceleration at nearly perpendicular

collisionless shocks. II - Reflection at curved shocks, *J. Geophys. Res.*, , *96*, 143–154, doi:10.1029/90JA01728.

- Krauss-Varban, D., and C. S. Wu (1989), Fast Fermi and gradient drift acceleration of electrons at nearly perpendicular collisionless shocks, *J. Geophys. Res.*, , *94*, 15,367–15,372, doi:10.1029/JA094iA11p15367.
- Krauss-Varban, D., D. Burgess, and C. S. Wu (1989), Electron acceleration at nearly perpendicular collisionless shocks. I - One-dimensional simulations without electron scale fluctuations, *J. Geophys. Res.*, , *94*, 15,089–15,098, doi:10.1029/JA094iA11p15089.
- Kuncic, Z., I. H. Cairns, and S. Knock (2002), Analytic model for the electrostatic potential jump across collisionless shocks, with application to Earth’s bow shock, *Journal of Geophysical Research (Space Physics)*, *107*, 1218, doi:10.1029/2001JA000250.
- Kuncic, Z., I. H. Cairns, and S. A. Knock (2004), A Quantitative model for terrestrial foreshock radio emissions: 1. Predicted properties, *Journal of Geophysical Research (Space Physics)*, *109*(A18), A02108, doi:10.1029/2003JA010125.
- Larson, D. E., et al. (1996), Probing the Earth’s bow shock with upstream electrons, *Geophys. Res. Lett.*, , *23*, 2203–2206, doi:10.1029/96GL02382.
- Lefebvre, B., S. J. Schwartz, A. F. Fazakerley, and P. Décréau (2007), Electron dynamics and cross-shock potential at the quasi-perpendicular Earth’s bow shock, *Journal of Geophysical Research (Space Physics)*, *112*(A11), A09212, doi:10.1029/2007JA012277.
- Lembège, B., and P. Savoini (2002), Formation of reflected electron bursts by the non-stationarity and nonuniformity of a collisionless shock front, *Journal of Geophysical Research (Space Physics)*, *107*, 1037, doi:10.1029/2001JA900128.
- Lembège, B., P. Savoini, P. Hellinger, and P. M. Trávníček (2009), Nonstationarity of a two-dimensional perpendicular shock: Competing mechanisms, *Journal of Geophysical Research (Space Physics)*, *114*(A13), A03217, doi:10.1029/2008JA013618.

- Leroy, M. M., and A. Mangeney (1984), A theory of energization of solar wind electrons by the earth's bow shock, *Annales Geophysicae*, *2*, 449–456.
- Lin, R. P. (1998), WIND Observations of Suprathermal Electrons in the Interplanetary Medium, *Space Sci. Rev.*, *86*, 61–78, doi:10.1023/A:1005048428480.
- Lin, R. P., et al. (1996), Observation of an impulsive solar electron event extending down to ~ 0.5 keV energy, *Geophys. Res. Lett.*, *23*, 1211–1214, doi:10.1029/96GL00710.
- Lin, R. P., et al. (2008), The STEREO IMPACT Suprathermal Electron (STE) Instrument, *Space Sci. Rev.*, *136*, 241–255, doi:10.1007/s11214-008-9330-7.
- Lobzin, V. V., V. V. Krasnoselskikh, J.-M. Bosqued, J.-L. Pinçon, S. J. Schwartz, and M. Dunlop (2007), Nonstationarity and reformation of high-Mach-number quasiperpendicular shocks: Cluster observations, *Geophys. Res. Lett.*, *34*, L05107, doi:10.1029/2006GL029095.
- Luhmann, J. G., et al. (2008), STEREO IMPACT Investigation Goals, Measurements, and Data Products Overview, *Space Sci. Rev.*, *136*, 117–184, doi:10.1007/s11214-007-9170-x.
- Maksimovic, M., V. Pierrard, and P. Riley (1997), Ulysses electron distributions fitted with Kappa functions, *Geophys. Res. Lett.*, *24*, 1151–1154, doi:10.1029/97GL00992.
- Malaspina, D. M., B. Li, I. H. Cairns, P. A. Robinson, Z. Kuncic, and R. E. Ergun (2009), Terrestrial foreshock Langmuir waves: STEREO observations, theoretical modeling, and quasi-linear simulations, *Journal of Geophysical Research (Space Physics)*, *114*(A13), A12101, doi:10.1029/2009JA014493.
- Malaspina, D. M., I. H. Cairns, and R. E. Ergun (2011), Dependence of Langmuir wave polarization on electron beam speed in type III solar radio bursts, *Geophys. Res. Lett.*,

, 38, L13101, doi:10.1029/2011GL047642.

Muschietti, L. (1990), Electron beam formation and stability, *Sol. Phys.*, 130, 201–228, doi:10.1007/BF00156790.

Ogilvie, K. W., et al. (1995), SWE, A Comprehensive Plasma Instrument for the Wind Spacecraft, *Space Sci. Rev.*, 71, 55–77, doi:10.1007/BF00751326.

Oka, M., et al. (2006), Whistler critical Mach number and electron acceleration at the bow shock: Geotail observation, *Geophys. Res. Lett.*, , 33, L24104, doi:10.1029/2006GL028156.

Oka, M., T. Terasawa, M. Fujimoto, H. Matsui, Y. Kasaba, Y. Saito, H. Kojima, H. Matsumoto, and T. Mukai (2009), Non-thermal electrons at the Earth’s bow shock: A ‘gradual’ event, *Earth, Planets, and Space*, 61, 603–606.

Opitz, A., et al. (2009), Temporal Evolution of the Solar Wind Bulk Velocity at Solar Minimum by Correlating the STEREO A and B PLASTIC Measurements, *Sol. Phys.*, 256, 365–377, doi:10.1007/s11207-008-9304-7.

Pierrard, V., and M. Lazar (2010), Kappa Distributions: Theory and Applications in Space Plasmas, *Sol. Phys.*, 267, 153–174, doi:10.1007/s11207-010-9640-2.

Pulupa, M., and S. D. Bale (2008), Structure on Interplanetary Shock Fronts: Type II Radio Burst Source Regions, *Astrophys. J.*, , 676, 1330–1337, doi:10.1086/526405.

Pulupa, M. P., S. D. Bale, and J. C. Kasper (2010), Langmuir waves upstream of interplanetary shocks: Dependence on shock and plasma parameters, *Journal of Geophysical Research (Space Physics)*, 115(A14), A04106, doi:10.1029/2009JA014680.

Pulupa, M. P., S. D. Bale, and C. Salem (2011), An asymmetry of the electron foreshock due to the strahl, *Geophys. Res. Lett.*, , 38, L14105, doi:10.1029/2011GL048029.

- Robinson, P. A., and A. O. Benz (2000), Bidirectional Type III Solar Radio Bursts, *Sol. Phys.*, *194*, 345–369.
- Sauvaud, J.-A., et al. (2008), The IMPACT Solar Wind Electron Analyzer (SWEA), *Space Sci. Rev.*, *136*, 227–239, doi:10.1007/s11214-007-9174-6.
- Savoini, P., and B. Lembège (2001), Two-dimensional simulations of a curved shock: Self-consistent formation of the electron foreshock, *J. Geophys. Res.*, , *106*, 12,975–12,992, doi:10.1029/2001JA900007.
- Savoini, P., B. Lembège, and J. Stienlet (2010), Origin of backstreaming electrons within the quasi-perpendicular foreshock region: Two-dimensional self-consistent PIC simulation, *Journal of Geophysical Research (Space Physics)*, *115*(A14), A09104, doi:10.1029/2010JA015263.
- Štverák, Š., M. Maksimovic, P. M. Trávníček, E. Marsch, A. N. Fazakerley, and E. E. Scime (2009), Radial evolution of nonthermal electron populations in the low-latitude solar wind: Helios, Cluster, and Ulysses Observations, *Journal of Geophysical Research (Space Physics)*, *114*(A13), A05104, doi:10.1029/2008JA013883.
- Vandas, M. (2001), Shock drift acceleration of electrons: A parametric study, *J. Geophys. Res.*, , *106*, 1859–1872, doi:10.1029/2000JA900128.
- Wang, L., et al. (2010), Energetic, ~ 5 -90 keV neutral atom imaging of a weak substorm with STEREO/STE, *Geophys. Res. Lett.*, , *37*, L08107, doi:10.1029/2010GL042964.
- Wang, L., R. P. Lin, C. S. Salem, and M. P. Pulupa (2012), Quiet-time Interplanetary ~ 2 -20 keV Superhalo Electrons at Solar Minimum, in preparation.
- Wu, C. S. (1984), A fast Fermi process - Energetic electrons accelerated by a nearly perpendicular bow shock, *J. Geophys. Res.*, , *89*, 8857–8862, doi:10.1029/JA089iA10p08857.

Xiao, F. (2006), Modelling energetic particles by a relativistic kappa-loss-cone distribution function in plasmas, *Plasma Physics and Controlled Fusion*, *48*, 203–213, doi: 10.1088/0741-3335/48/2/003.

Zimbardo, G., and P. Veltri (1996), Spreading and intermittent structure of the upstream boundary of planetary magnetic foreshocks, *Geophys. Res. Lett.*, , *23*, 793–796, doi: 10.1029/96GL00660.

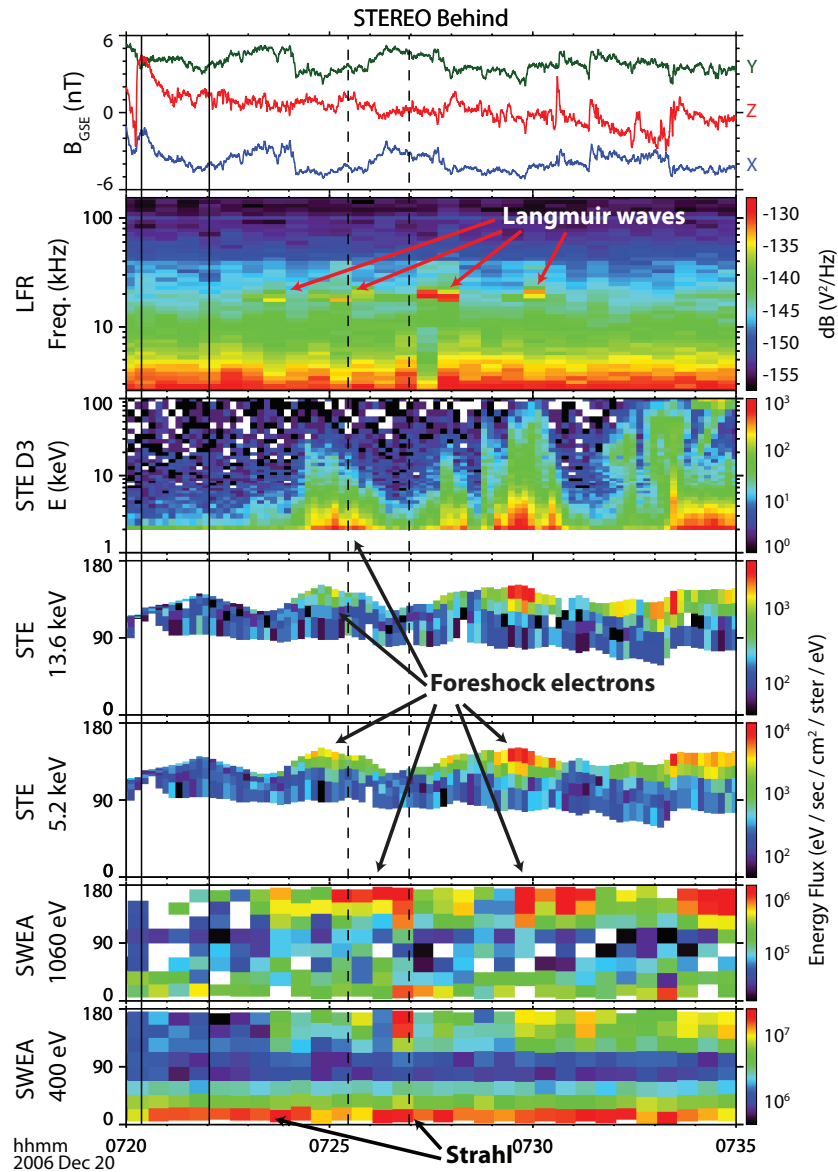


Figure 1. Upstream foreshock electron event observed by STEREO/Behind on 20 December 2006. From top to bottom, the plotted quantities are: GSE magnetic field, electric field spectrogram from S/WAVES LFR, energy spectrogram from the STE D3 detector, STE PADs at 13.6 keV and 5.2 keV, and SWEA PADs at 1060 eV and 400 eV. The foreshock electrons are visible in the STE spectrogram starting at around 7:25 UT. The PADs for the electrons show enhancements in the antiparallel direction corresponding to foreshock electron beams. The time interval delineated by the two vertical bars near 7:20 UT is used to calculate the incident eVDF. The time intervals near 7:25 and 7:27 UT correspond to the two foreshock intervals analyzed in

Section 5.

D R A F T

February 17, 2012, 4:16am

D R A F T

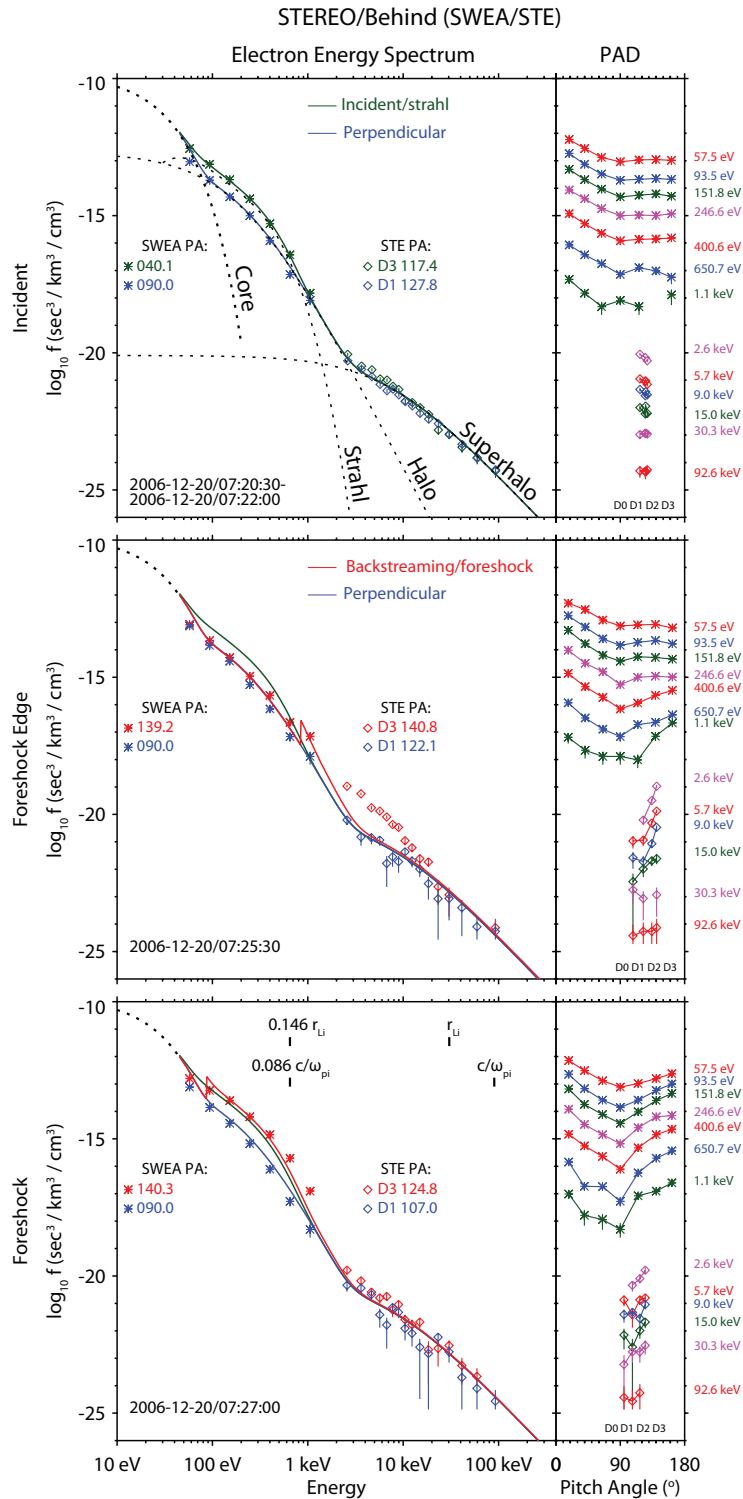


Figure 2. Energy spectra and PADs for the incident electrons (top row) and the foreshock electron beams at the foreshock edge (middle row) and deeper in the foreshock (bottom row). SWEA pitch angle bins are marked by asterisks, and STE bins are marked by diamonds. A full description of this figure can be found in Sections 3 and 5 of the text.

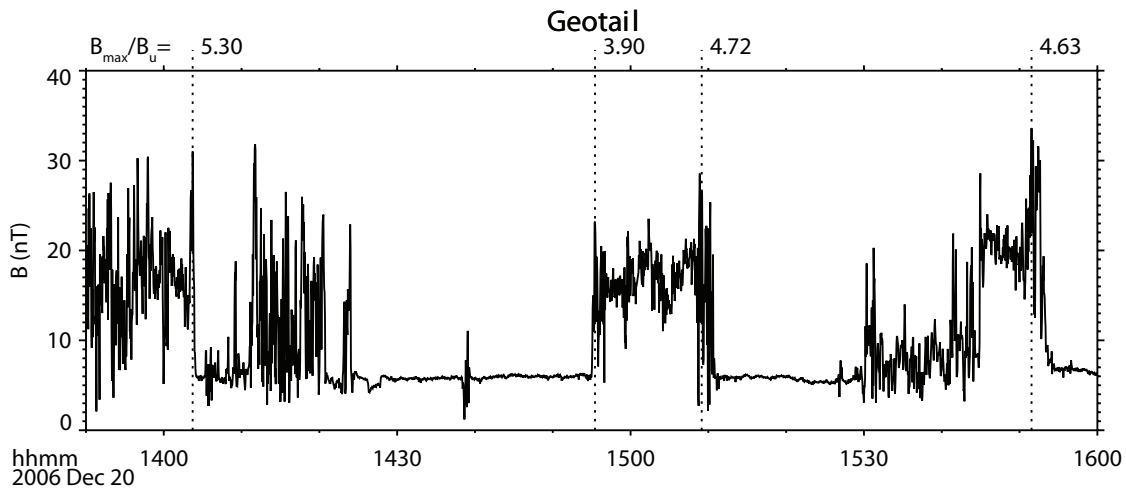


Figure 3. Several crossings of the quasiperpendicular bow shock as observed by Geotail on 20 December 2006. Geotail crossed the shock near the electron acceleration site for the event observed by STEREO/B. The crossings are indicated by dotted lines. For each analyzed crossing, the ratio B_{\max}/B_u is shown. A full description of this figure can be found in Section 4.1.

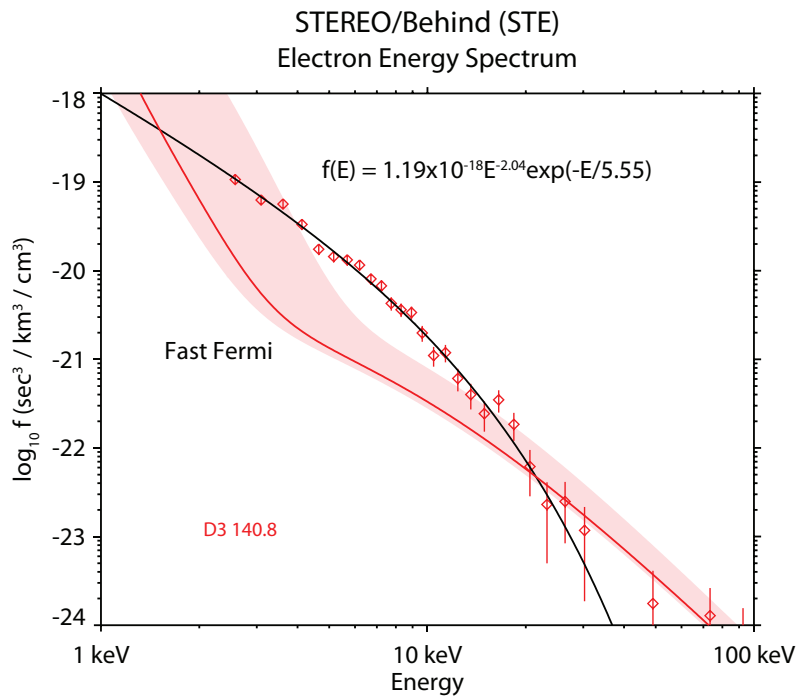


Figure 4. STE energy spectrum for the foreshock edge electron beam, demonstrating significant enhancement of accelerated electrons compared to the Fast Fermi theory. The spectrum is well fit by a power law with an exponential roll off (black solid line). The red line and the red shaded area show the range of predicted spectra calculated using Liouville's theorem and the fast Fermi acceleration mechanism. A full description of this figure can be found in Section 5.1.

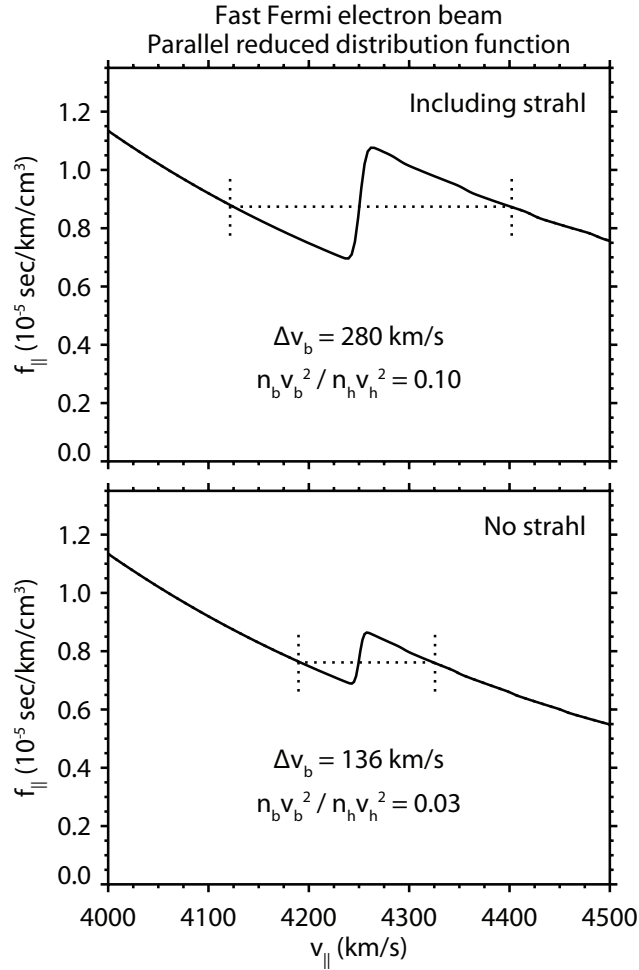


Figure 5. Reduced parallel distribution f_{\parallel} from the Liouville mapping. The solid line in the upper plot shows f_{\parallel} calculated using the parameters described in Sections 3 and 4.1. The large bump on tail is a result of the strong strahl population in the incident eVDF. The horizontal dotted line represents the relaxed plateau distribution constructed by eliminating the bump on tail while conserving particle number, as described in Section 4.3. The lower plot shows the results of the same procedure with the strahl removed from the incident eVDF, with the result that the bump is significantly smaller. A full description of this figure can be found in Section 5.4.

n_c	4.72 cm ⁻³
T_c	8.82 eV
n_h	0.065 cm ⁻³
T_h	48.6 eV
κ_h	5.9
n_{sh}	0.731×10^{-6} cm ⁻³
T_{sh}	2.50 keV
κ_{sh}	2.7

Table 1. Measured parameters for the incident eVDF. The field-aligned strahl component is fit empirically using a spline fit and not to a parameterized model.

α	27.7°
Φ	72. eV
v_{HT} (foreshock edge)	1500 km/s
v_{HT} (deeper foreshock)	500 km/s
v_c (foreshock edge)	13000 km/s
v_c (deeper foreshock)	4250 km/s

Table 2. Parameters used to calculate the Liouville mapping of electrons through the fast Fermi shock encounter. These parameters are estimated using upstream plasma measurements and Geotail shock crossings. See Section 4.1 for a complete description of parameter estimation.